PHOTONICS Research

Integrated dispersion compensated mode-locked quantum dot laser

Zeyu Zhang,[1,2,*] Justin C. Norman,[2] Songtao Liu,[3] Aditya Malik,[1] and John E. Bowers[1,2,3]

[1]Electrical and Computer Engineering Department, University of California Santa Barbara, Santa Barbara, California 93106, USA
[2]Materials Department, University of California Santa Barbara, Santa Barbara, California 93106, USA
[3]Institute for Energy Efficiency, University of California, Santa Barbara, California 93106, USA
*Corresponding author: z_zhang@ucsb.edu

Received 8 May 2020; revised 17 June 2020; accepted 30 June 2020; posted 7 July 2020 (Doc. ID 397175); published 7 August 2020

Quantum dot lasers are excellent on-chip light sources, offering high defect tolerance, low threshold, low temperature variation, and high feedback insensitivity. Yet a monolithic integration technique combining epitaxial quantum dot lasers with passive waveguides has not been demonstrated and is needed for complex photonic integrated circuits. We present here, for the first time to our knowledge, a monolithc offset quantum dot integration platform that permits formation of a laser cavity utilizing both the robust quantum dot active region and the versatility of passive GaAs waveguide structures. This platform is substrate agnostic and therefore compatible with the quantum dot lasers directly grown on Si. As an illustration of the potential of this platform, we designed and fabricated a 20 GHz mode-locked laser with a dispersion-engineered on-chip waveguide mirror. Due to the dispersion compensation effect of the waveguide mirror, the pulse width of the mode-locked laser is reduced by a factor of 2.8.

https://doi.org/10.1364/PRJ.397175

1. INTRODUCTION

Quantum dot (QD) lasers bring several distinct advantages over their quantum well (QW) counterparts. First proposed in 1982 as temperature-insensitive lasers [1], QD lasers hold the record for highest continuous-wave (CW) operating temperature (220°C) due to the dots having discrete energy levels [2]. The reduced density of states gives rise to reduced transparency carrier density, which translates to low threshold current [3]. The atom-like dot structure possesses a symmetric delta-like gain spectrum, which corresponds to near-zero linewidth enhancement factor [4]. This in turn manifests as optical feedback insensitivity and ultranarrow linewidth [5,6].

Perhaps the most notable characteristic of the QD lasers is their high tolerance to growth defects due to locally confined carrier in each dot [7]. Such high tolerance enables epitaxial growth of QD material on CMOS-compatible substrates, such as on-axis (001) silicon (Si). Epitaxial growth on large Si substrates brings the benefits of significantly reduced cost and potential high-density integration of QD lasers in photonic integrated circuits (PICs) [8]. Significant progress has been made in this direction in the past few years for QD lasers grown on Si, with reliability and laser performance approaching those of QD lasers grown on native substrate [7,9,10]. A variety of devices have been demonstrated including Fabry–Perot (FP) lasers, distributed feedback (DFB) lasers [11], mode-locked lasers (MLLs) [12], microring lasers [13], coupled cavity tunable lasers [14], and photodetectors (PDs) [15].

Yet, all the aforementioned devices are stand-alone devices, and no integration of such devices with monolithic PICs has been reported. This issue stems from the lack of a passive waveguide (WG) in the current epitaxial QD on the Si device platform. Indeed, the versatility of passive WG structures is imperative in building successful laser integration platforms, as in the case of InP PICs [16], heterogeneous III-V on Si PICs [17], or recent heterogeneous III-V/Si/Si_3N_4 PICs [18]. In the QD laser on a Si platform, proposals for integration with Si WGs have been made [7,8]. One of them suggests coupling light from laser active region downward through several micrometers of III-V buffer layers to reach the Si layer; the other requires growing QD lasers in a trench and aligning the active WG with the passive WG in height. Both are challenging in terms of growth and optical coupling element design. Another approach involves heterogeneous integration of QDs on a silicon-on-insulator (SOI) wafer via direct bonding. This approach is readily achievable given that lasers from bonding of native substrate QD lasers on SOI wafers have already been demonstrated [19]. However, our goal is scaling the entire process to 300 mm Si wafers and achieve the ultimate cost efficiency [20].

Here we showcase a novel passive-active integration scheme for QD on Si, which we term the offset quantum dot (OQD)

device platform. The concept is similar to the offset quantum well (OQW) technique widely used in InP PICs [21]. Both approaches involve shifting the active regions upward from the center of the intrinsic region of the laser epitaxy. By doing so, the lower half of the intrinsic region can be utilized as a passive WG layer to form a laser cavity or other passive WG structures for light partitioning, routing, or switching purposes. The differences of the OQD scheme from its QW counterparts are twofold. First, instead of multiple regrowths, the OQD approach fully establishes all the contact and passive layers within a single epitaxy growth, significantly simplifying the fabrication procedure. Second, the QD active region's thickness (>200 nm) is considerably larger than that of QW active region (~100 nm). This results in much larger optical mode mismatch between the active and passive WGs in OQD devices, necessitating careful design of the active-passive WG transition, not existing in offset QW devices. The OQD platform is able to scale with the size of the cheap Si substrate by fully exploiting the cost reduction of larger wafer size. Furthermore, the OQD platform benefits from a simple fabrication flow that does not require multiple regrowths as in the monolithic InP laser platform or wafer bonding as in the heterogeneous laser platform, further facilitating cost saving. To demonstrate the potential of the OQD device platform, we design and fabricate the first epitaxial passively mode-locked OQD lasers. These lasers have one mirror formed by sidewall gratings etched on the passive GaAs WG. These gratings are chirped and apodized to compensate for the group velocity dispersion generated in the active section of the lasers. These lasers have a repetition rate designed at 20 GHz. The minimum threshold is 58 mA with saturable absorber (SA) left floating. The minimum pulse width is 4.5 ps, representing a factor of 2.8 reduction compared to MLLs without dispersion compensation.

2. EPITAXY DESIGN AND DEVICE FABRICATION

The InAs OQD laser growth is performed on a native GaAs substrate by solid-source molecular beam epitaxy. Although the OQD platform is primarily designed for QD lasers on Si, as will be shown later, the fabrication procedure is entirely substrate agnostic and can readily be implemented on lasers grown on any substrate. Figure 1(a) shows the detailed QD epitaxial structure. The laser epitaxy is similar to what has been detailed in Ref. [10] with several distinctions in the intrinsic region. The growth starts with a 500 nm heavily n-type doped GaAs contact layer and a 1400 nm n-type AlGaAs cladding layer. 30 nm of $Al_{0.2}Ga_{0.8}As$ follows the n-type cladding to function as the second etch stop during fabrication. It was then followed by 230 nm of intrinsic GaAs WG layer and another 20 nm of $Al_{0.2}Ga_{0.8}As$ as the first etch stop during fabrication. Afterward, five layers of InAs/$In_{0.15}Ga_{0.85}As$ dots-in-a-well (DWELLs) active regions with 37.5 nm GaAs spacers are grown. A 10 nm 5×10^{17} cm^{-3} p-modulation-doped GaAs layer was also introduced to each spacer to help improve the gain and temperature performance of the laser. The thick GaAs spacer layers are the main reason for the considerably larger passive-active WG mode mismatch in OQD devices compared to OQW devices. After the active region deposition, the whole growth procedure is completed with a 1400 nm p-type AlGaAs cladding and a 300 nm heavily doped p-type GaAs contact layer. The photoluminescence spectrum is centered at 1267 nm with a full width at half-maximum (FWHM) of 56 nm corresponding to inhomogeneous broadening 17 meV [22]. The dependence of optical confinement on the thickness of the passive GaAs WG is shown in Fig. 1(b). When the passive GaAs is 50 nm, the epitaxial structure is almost identical to the previously reported QD lasers [9,10], with the exception of the thin etch stop A. Thicker GaAs WG in OQD dilutes the optical confinement in the DWELLs. However, since the optical mode becomes more confined in the intrinsic region, the decrease in confinement in the DWELLs when the GaAs WG layer is 230 nm is only ~20%, despite the doubling of intrinsic region volume. When the GaAs WG layer is thinner than 230 nm, the mode overlap with the highly doped n-contact layer becomes large enough to make the optical loss significant in the passive WG. The larger minimum bending radius resulting from a thinner passive GaAs WG core also enlarges device footprints. Balancing these trade-offs, a design choice is made to set the passive GaAs WG layer thickness to be 230 nm.

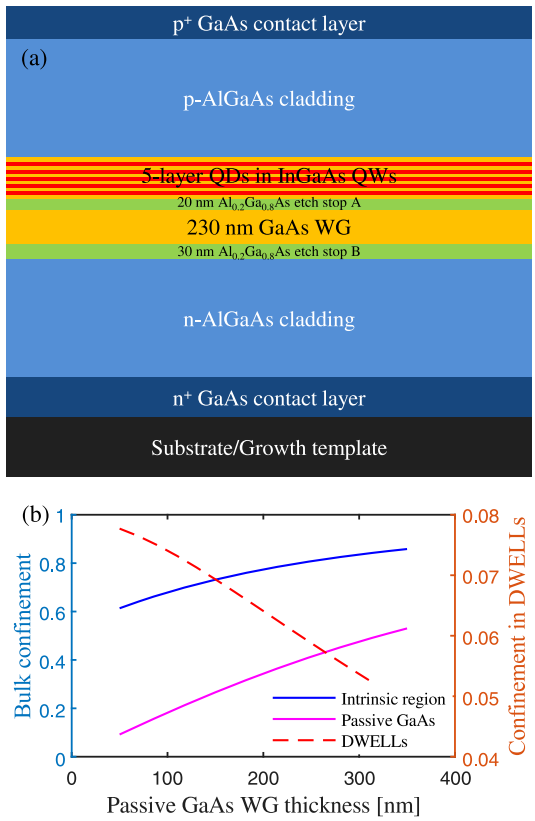

Fig. 1. (a) Schematic diagram of the epitaxial structure of OQD devices. (b) Optical confinement as functions of passive GaAs WG thickness.

OQD devices were fabricated on a quarter of a 3 inch (76 mm) GaAs wafer after molecular beam epitaxy (MBE) growth. First, the mesa pattern of the active section is defined by an oxide hard mask with i-line lithography, which is used throughout the fabrication process except as otherwise mentioned. The pattern is then transferred down to the III-V material with

a two-step inductively coupled plasma reactive ion etch (ICP-RIE). This two-step ICP-RIE process aims to remove all the active material above the first etch stop layer outside of the mesa region. The first ICP-RIE step uses a nonselective Cl_2/N_2 etch chemistry that stops ~100 nm above the first etch stop assisted by a laser etch monitor [Fig. 2(b)]. The second ICP-RIE step uses a highly selective $BCl_3/SF_6/N_2$ etch chemistry that precisely stops the etch on the first $Al_{0.2}Ga_{0.8}As$ etch stop layer sandwiched between the active regions and the GaAs passive WG layer. This etch recipe [23] is optimized to have GaAs to $Al_{0.2}Ga_{0.8}As$ etch selectivity of 20 to 1, with $Al_{0.2}Ga_{0.8}As$ etch rate of 3 nm/min. It cannot be stressed enough that having this selective etch is crucial to the success of this OQD laser platform. Had only the nonselective etch been used for defining the ~2000 nm deep mesa, the etch nonuniformity would cause either residual QD layers on top of the GaAs WG or significantly over-etched WG layer. Both results are conducive to large WG propagation loss and variation of WG dimensions across the wafer. After the mesa etch, electron beam lithography and i-line lithography are used to define the grating and WG pattern, respectively, on the same oxide hard mask. Redundancy has been included in the grating pattern to provide tolerance to misalignment in the i-line lithography. The combined grating and WG pattern is then used to etch the WG structure, utilizing the same ICP-RIE steps detailed earlier, stopping on the second $Al_{0.2}Ga_{0.8}As$ etch stop [Figs. 2(c) and 2(d)]. Afterward, the isolation between the SA and the gain section is created. Trenches around the mesa are etched to give access to the n-type contact. The last steps in fabrication are passivation and metalization to form contacts. The two etch stops guarantee precise and uniform WG dimensions across the wafer while eliminating the micro-trenching caused by the nonselective etch as seen in Fig. 2(b). Altogether, the OQD device platform is well poised for future development of flexible and variation-tolerant WG structures.

3. DEVICE DESIGN AND SIMULATION

A schematic representation of the MLL design is shown in Fig. 2(a). The laser primarily consists of four sections: an SA adjacent to a cleaved facet, a gain section with the passive-active transition taper, a short GaAs WG, and a grating mirror terminated by a WG spiral. The effective length of the laser is defined as the length of the first three sections of the laser plus the effective length of the grating. To achieve 20 GHz repetition rate, the effective length of the laser is set to be 2050 μm. The SA is set to be 20% of the effective cavity length. Special attention has been given to the active-passive taper transition in the laser design. The width of the mesa is set to be 3.5 μm, which is wide enough to avoid sidewall recombination [24]. The taper tip width is 0.5 μm, which can be reliably achieved by i-line lithography. The standard WG width is chosen to be 1.6 μm to maximize the optical confinement while maintaining a single-mode condition. In the taper gain section defined by the mesa etch, the mesa width is linearly varied over a length of 50 μm. During this transition, 10 μm from the taper tip, the WG layer linearly widens to 1.8 μm at the taper tip [Fig. 2(e)]. Afterward, the GaAs WG is tapered down to the standard width over 20 μm. The widened passive WG around the taper not only facilitates a downward optical power transition but also helps relax the alignment constraint between the two mask layers during fabrication. Finite-difference time-domain (FDTD) simulation has shown 1.4 dB passive transmission loss and -15 dB reflection for the aforementioned taper design.

For successful operation of the QD MLL, proper design of the grating mirror is important. Given the same time-bandwidth product (TBP), wider lasing bandwidth leads to shorter pulses. However, pulses from stand-alone semiconductor MLLs are always chirped due to self-phase modulation [25]. The dispersion in the gain section and the SA also reduces the locking bandwidth of an MLL, further broadening the pulse. Passive elements such as WG [26] or fiber [27] gratings have been integrated with QW MLLs to compensate for the dispersion generated by the active components. In QW MLLs, experimental investigations have found red-chirped pulses generated by active mode locking [26–29] and pulses in both chirping directions from passive mode locking [30–32]. For red-chirped pulses, negatively chirped gratings are required

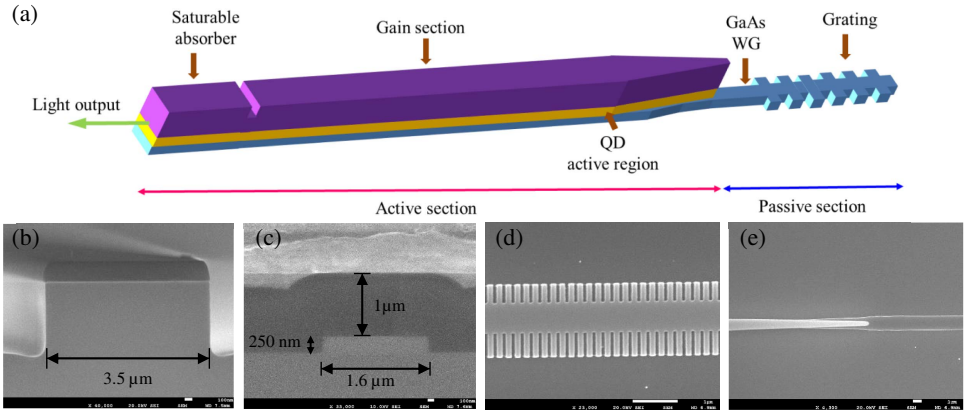

Fig. 2. (a) Schematic diagram of OQD MLL above the bottom cladding. The rendering is not to scale. The WG spiral termination is not illustrated here for simplicity. Scanning electron microscope (SEM) images of (b) mesa cross section after the nonselective GaAs etch, (c) passive GaAs WG cross section with 1 μm thick silicon dioxide upper cladding, (d) GaAs WG with gratings etched on the sidewall, and (e) taper transition from the active to the passive WG section.

to provide longer effective length for the blue end of the spectrum in order to compress the pulse. For blue-chirped pulses, the opposite is true. For QD MLLs, reports have shown red-chirped output from the gain section [33] with the contribution from the SA being negligible [34]. Based on this information, an apodized and negatively chirped WG grating has been designed. The total length of the grating is 200 μm. To chirp the grating, the average effective index of the WG is varied so that the Bragg condition of the grating changes at a chirp rate (CR) of −0.032 nm/μm. The negative sign indicates decreasing local Bragg wavelength in the direction away from the gain section. Apodization is implemented by modulating both the inner and outer profiles of the grating recesses with a Gaussian function, so that the average WG effective index profile still conforms to that required to achieve the desired chirp rate [35]. The reflectivity and group delay responses of the grating designs have been studied with a transmission matrix model implemented in MATLAB. The results are plotted in Fig. 3. As can be seen, the uniform grating offers no compensation in the group delay, while all the negatively chirped gratings generate more delay in the blue side of the spectrum around the Bragg wavelength. The necessity of apodization is apparent from the ripples in the pink curve in Fig. 3(a). These ripples degrade the flatness within the stopband of the grating, limiting the locking bandwidth of the MLL. These ripples are largely eliminated from the implementation of the Gaussian apodization profile in the gratings represented by the blue curve, at the price of less group delay dispersion. This can be compensated by making the gratings stronger as seen in the green curve in Fig. 3(b). During the mask layout, MLLs with different grating strengths and chirp directions are implemented to quantify the impact of the grating designs.

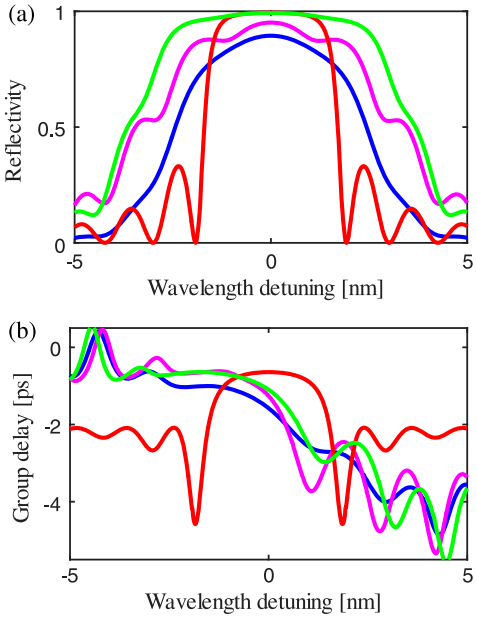

Fig. 3. (a) Reflectivities and (b) group delay responses of several grating designs simulated with the transmission matrix technique. Red: uniform grating, $\kappa = 162\ \mathrm{cm}^{-1}$. Pink: linearly chirped grating, CR = −0.032 nm/μm. Blue and green: chirped and apodized gratings, CR = −0.032 nm/μm. For pink and blue, $\kappa = 162\ \mathrm{cm}^{-1}$ at the half length of the grating. For green, $\kappa = 243\ \mathrm{cm}^{-1}$ at the half length.

4. CHARACTERIZATION AND DISCUSSION

The fabricated 20 GHz QD MLL chips are mounted on a copper heat sink and tested at a fixed stage temperature of 18°C. CW light-current-voltage (LIV) characteristics are first measured as shown in Fig. 4(a). The light is collected from the cleaved facets using an integration sphere. Attention is focused on three laser designs: laser A with uniform grating, $\kappa = 260\ \mathrm{cm}^{-1}$; laser B with apodized and positively chirped grating, CR = 0.032 nm/μm; laser C with apodized and negatively chirped grating, CR = −0.032 nm/μm. Lasers B and C both have $\kappa = 260\ \mathrm{cm}^{-1}$ at half-length of the grating. The steps at the laser thresholds are from the loss-bleaching effect in the SAs as intracavity power increases. All lasers have similar series resistance around 3.3 Ω. Compared to previous QD MLL lasers of similar length [12], these lasers show 10–20 mA higher threshold current. This is due to the additional optical loss and carrier surface recombination introduced by the taper transition between the active and passive WGs, warranting further optimization of the taper design. Among the three lasers, laser B and laser C have the lowest and highest threshold current, respectively. The positively chirped grating exhibits reflection peak at 1292 nm as opposed to 1293 nm for uniform grating and 1297 nm for negatively chirped grating. The differences in misalignment between the laser gain peaks and the grating reflection peaks explain the observed threshold differences.

To study the passive mode-locking (PML) behavior of the laser, the output spectrum was measured using an optical spectrum analyzer (Yokogawa, AQ6370C), RF performance was measured with an electrical spectrum analyzer (Rohde & Schwarz, FSU), and the autocorrelation pulse width was

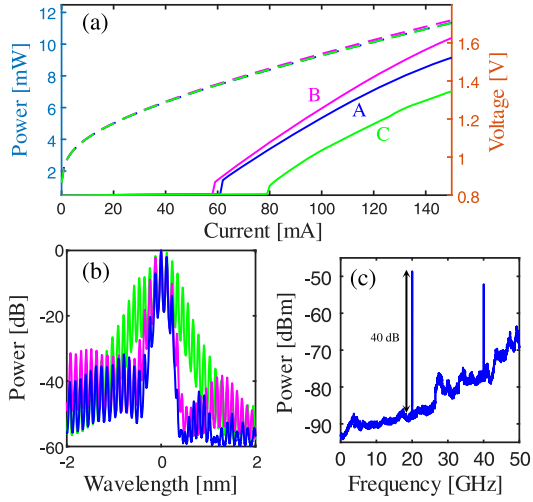

Fig. 4. (a) CW LIV curves for 20 GHz OQD MLL with SA in a floating state. Blue: laser A. Pink: laser B. Green: laser C. (b) Optical spectra under the bias conditions I_{gain} = 129 mA, 179 mA, 94 mA and V_{SA} = 5.6 V, 2.7 V, 4.3 V for lasers A–C, respectively. (c) RF spectrum for laser C under the same bias condition in 50 GHz span view.

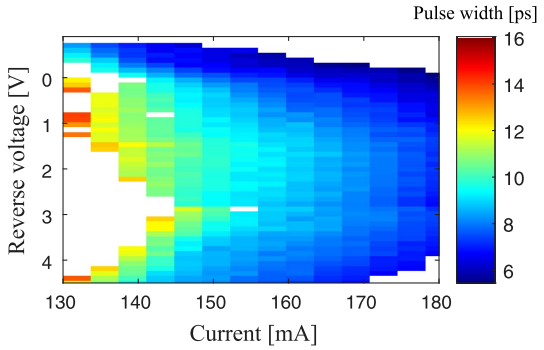

Fig. 5. Pulse width mapping as a function of gain section current and SA section reverse bias voltage under passive mode-locking operation for laser C. Regions marked by white indicate unsuccessful PML.

recorded with an autocorrelator (Femtochrome, FM-103MN). The light is collected from the cleaved facet with a lensed fiber. The optical spectra under the conditions for the narrowest pulses are shown in Fig. 4(b) for lasers A–C. The dispersion compensation effect of the negatively chirped grating can be immediately seen from the broadened PML bandwidth in laser C. The 3 dB (10 dB) bandwidths for lasers A and C are 0.15 nm (0.28 nm) and 0.4 nm (0.9 nm), accommodating 2 (2) and 3 (8) lines. Lasers A and B have similar locking bandwidth. However, as will be shown later, positively chirped

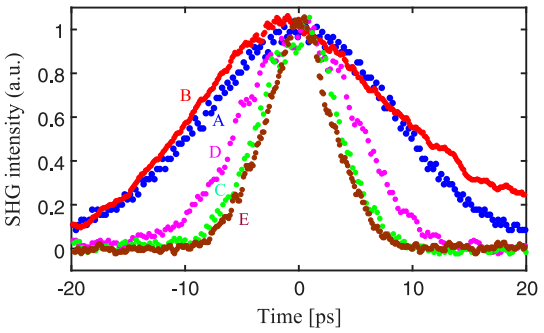

Fig. 6. (a) Autocorrelator traces of the narrowest pulses of OQD MLLs with various grating designs. Blue, red, green, pink, and brown circles represent lasers A–E, respectively. Sech^2 fitting gives pulse widths of 12.8, 14.4, 5.3, 7.6, and 4.5 ps. The bias conditions for narrowest pulses are $I_{gain} = 129$ mA, 179 mA, 94 mA, 108 mA, 101 mA and $V_{SA} = 5.6$ V, 2.7 V, 4.3 V, 0 V, 6.2 V, for lasers A–E, respectively.

grating increases the time-bandwidth product, resulting in broadened pulse. The RF performance for laser C under the bias condition for the narrowest pulse is shown in Fig. 4(c). A sharp fundamental RF tone at 20.01 GHz with a signal-to-noise ratio (SNR) of 40 dB and the second harmonic can be clearly seen across the 50 GHz span. The other lasers also have fundamental RF tones near 20 GHz with comparable SNR.

The PML regime of the dispersion-compensated OQD MLL is also thoroughly examined by measuring the pulse width as a function of gain section forward biased current and SA section reverse biased voltage. For laser C, a wide mode-locking area is demonstrated with forward current ranging from 130 to 180 mA and reverse voltage ranging from −0.9 to 4.3 V as shown in Fig. 5. This is vastly better compared to lasers A and B, whose mode-locking regimes are not continuous. Two interesting observations can be made from this figure. First, the laser appears to mode lock even when the SA is forward biased, proving the feasibility of single-section OQD MLLs as has been predicted before [36]. Second, the pulse width reduces with increasing current applied to the gain section, with the lowest pulse width occurring right before the mode-locking stops. This is likely due to the walk-off between the gain peak and grating reflection peak as the gain section continues to self-heat. By having a heater on the grating section, this walk-off phenomenon may be mitigated, helping the laser to generate even narrower pulse width. Similar walk-off also happens when the stage temperature is varied. In this case both gain peak and grating reflection peak shift with changing temperature, albeit at different rates. This causes the temperature dependence of lasing threshold to be no longer monotonic. Instead, an optimum temperature for lowest threshold exists for each grating design.

To compare the effects of different grating designs, the autocorrelator traces of the narrowest pulses from several MLLs are plotted together in Fig. 6. In addition to lasers A–C introduced before, laser D has negatively chirped grating with CR = −0.016 nm/μm and $\kappa = 260$ cm^{-1} at half-length; laser E has negatively chirped grating with CR = −0.032 nm/μm and $\kappa = 350$ cm^{-1} at half-length. In contrast to laser C, the grating mirror on laser B broadens the pulse due to the exacerbated group delay dispersion as expected from the positively chirped grating. Furthermore, the narrowest pulses decrease as the CR decreases in lasers B, A, D, and C, in that order. This proves that not only the direction but also the rate matters in the chirped grating for dispersion compensation. Based on the observed trend, a more negative CR is desirable to reach even narrower pulses. As predicted in Fig. 3, a stronger grating compensates for the desired group delay dispersion lost

Table 1. MLL Design and Performance Parameters

	MLL A	MLL B	MLL C	MLL D	MLL E
Apodization	None	Gaussian	Gaussian	Gaussian	Gaussian
CR (nm/μm)	0	0.032	−0.032	−0.016	−0.032
κ at grating center (cm^{-1})	260	260	260	260	350
Threshold current (mA)	61	58	79	83	91
Wavelength at grating reflection peak (nm)	1293.1	1292.1	1297.2	1295.2	1288.4
Minimum pulse width (ps)	12.8	14.4	5.3	7.6	4.5

during apodization. This can be readily verified by comparing lasers C and E. Indeed, the strong grating in laser E helps generate the narrowest pulse in all tested OQD MLLs, resulting in a factor of 2.8 improvement compared to laser A. To achieve strong κ in laser E, the grating recess is increased. Consequently, the average effective index of the grating decreases, causing significant blueshift of the grating reflection peak as shown in Table 1. Decreased effective index also means less WG confinement in GaAs and more mode overlap with the doped n-type cladding. The large grating recess also leads to more interaction between the optical mode and WG surfaces. These observations explain the increased threshold current in laser E. A deeply etched grating provides a good alternative to increase κ without these drawbacks.

5. CONCLUSION

We have designed and demonstrated a novel passive-active integration scheme for QD lasers on Si based on an offset quantum dot device platform. This platform is enabled by the development of a GaAs/AlGaAs selective etch, which ensures uniform WG geometries and eliminates the need for regrowth. The transition between the passive and active WGs is accomplished by a linear taper, whose design requires further investigation to reduce taper losses. The potential of the OQD device platform is illustrated by the successful integration of the MLL active sections with dispersion-engineered gratings etched on the passive WGs. The experiment has shown that negatively chirped and apodized grating mirrors can compensate for the group delay dispersion generated by the active sections of the MLLs. By carefully designing the chirp rate and grating strength, a factor of 2.8 reduction in pulse width has been achieved. More investigations will be carried out using the frequency-resolved optical gating (FROG) technique to further assist the design and characterization of the chirped gratings. The next important step for the OQD platform development will be the demonstration of integrated OQD PICs on Si substrate. As the OQD platform matures, we expect more OQD laser devices such as distributed Bragg reflector (DFB) lasers, DBR lasers, and sampled grating distributed Bragg reflector (SGDBR) lasers, to be implemented in the future.

Funding. Advanced Research Projects Agency-Energy (DE-AR0001039).

Disclosures. The authors declare no conflicts of interest.

REFERENCES

1. Y. Arakawa and H. Sakaki, "Multidimensional quantum well laser and temperature dependence of its threshold current," Appl. Phys. Lett. **40**, 939–941 (1982).
2. T. Kageyama, K. Nishi, M. Yamaguchi, R. Mochida, Y. Maeda, K. Takemasa, Y. Tanaka, T. Yamamoto, M. Sugawara, and Y. Arakawa, "Extremely high temperature (220°C) continuous-wave operation of 1300-nm-range quantum-dot lasers," in *European Conference on Lasers and Electro-Optics* (Optical Society of America, 2011), paper PDA_1.
3. D. Bimberg and U. W. Pohl, "Quantum dots: promises and accomplishments," Mater. Today **14**, 388–397 (2011).
4. J. Duan, H. Huang, D. Jung, Z. Zhang, J. Norman, J. Bowers, and F. Grillot, "Semiconductor quantum dot lasers epitaxially grown on silicon with low linewidth enhancement factor," Appl. Phys. Lett. **112**, 251111 (2018).
5. H. Huang, J. Duan, D. Jung, A. Y. Liu, Z. Zhang, J. Norman, J. E. Bowers, and F. Grillot, "Analysis of the optical feedback dynamics in InAs/GaAs quantum dot lasers directly grown on silicon," J. Opt. Soc. Am. B **35**, 2780–2787 (2018).
6. Z. Zhang, D. Jung, J. C. Norman, W. W. Chow, and J. E. Bowers, "Linewidth enhancement factor in InAs/GaAs quantum dot lasers and its implication in isolator-free and narrow linewidth applications," IEEE J. Sel. Top. Quantum Electron. **25**, 1900509 (2019).
7. A. Y. Liu, S. Srinivasan, J. Norman, A. C. Gossard, and J. E. Bowers, "Quantum dot lasers for silicon photonics," Photon. Res. **3**, B1–B9 (2015).
8. J. C. Norman, D. Jung, Y. Wan, and J. E. Bowers, "Perspective: the future of quantum dot photonic integrated circuits," APL Photon. **3**, 030901 (2018).
9. S. Chen, W. Li, J. Wu, Q. Jiang, M. Tang, S. Shutts, S. N. Elliott, A. Sobiesierski, A. J. Seeds, and I. Ross, "Electrically pumped continuous-wave III-V quantum dot lasers on silicon," Nat. Photonics **10**, 307–311 (2016).
10. D. Jung, Z. Zhang, J. Norman, R. Herrick, M. Kennedy, P. Patel, K. Turnlund, C. Jan, A. C. Gossard, and J. E. Bowers, "Highly reliable low-threshold InAs quantum dot lasers on on-axis (001) Si with 87% injection efficiency," ACS Photon. **5**, 1094–1100 (2017).
11. Y. Wang, S. Chen, Y. Yu, L. Zhou, L. Liu, C. Yang, M. Liao, M. Tang, Z. Liu, and J. Wu, "Monolithic quantum-dot distributed feedback laser array on silicon," Optica **5**, 528–533 (2018).
12. S. Liu, X. Wu, D. Jung, J. C. Norman, M. Kennedy, H. K. Tsang, A. C. Gossard, and J. E. Bowers, "High-channel-count 20 GHz passively mode-locked quantum dot laser directly grown on Si with 4.1 Tbit/s transmission capacity," Optica **6**, 128–134 (2019).
13. Y. Wan, J. Norman, Q. Li, M. Kennedy, D. Liang, C. Zhang, D. Huang, Z. Zhang, A. Y. Liu, and A. Torres, "1.3 μm submilliamp threshold quantum dot micro-lasers on Si," Optica **4**, 940–944 (2017).
14. Y. Wan, S. Zhang, J. C. Norman, M. Kennedy, W. He, S. Liu, C. Xiang, C. Shang, J.-J. He, A. C. Gossard, and J. E. Bowers, "Tunable quantum dot lasers grown directly on silicon," Optica **6**, 1394–1400 (2019).
15. Y. Wan, Z. Zhang, R. Chao, J. Norman, D. Jung, C. Shang, Q. Li, M. Kennedy, D. Liang, C. Zhang, J.-W. Shi, A. C. Gossard, K. M. Lau, and J. E. Bowers, "Monolithically integrated InAs/InGaAs quantum dot photodetectors on silicon substrates," Opt. Express **25**, 27715–27723 (2017).
16. S. Arafin and L. A. Coldren, "Advanced InP photonic integrated circuits for communication and sensing," IEEE J. Sel. Top. Quantum Electron. **24**, 6100612 (2017).
17. T. Komljenovic, M. Davenport, J. Hulme, A. Y. Liu, C. T. Santis, A. Spott, S. Srinivasan, E. J. Stanton, C. Zhang, and J. E. Bowers, "Heterogeneous silicon photonic integrated circuits," J. Lightwave Technol. **34**, 20–35 (2016).
18. C. Xiang, W. Jin, J. Guo, J. D. Peters, M. Kennedy, J. Selvidge, P. A. Morton, and J. E. Bowers, "Narrow-linewidth III-V/Si/Si_3N_4 laser using multilayer heterogeneous integration," Optica **7**, 20–21 (2020).
19. G. Kurczveil, C. Zhang, A. Descos, D. Liang, M. Fiorentino, and R. Beausoleil, "On-chip hybrid silicon quantum dot comb laser with 14 error-free channels," in *2018 IEEE International Semiconductor Laser Conference (ISLC)* (IEEE, 2018), pp. 1–2.
20. A. Y. Liu and J. Bowers, "Photonic integration with epitaxial III-V on silicon," IEEE J. Sel. Top. Quantum Electron. **24**, 6000412 (2018).
21. H. Zhao, S. Pinna, B. Song, L. Megalini, S. T. Š. Brunelli, L. A. Coldren, and J. Klamkin, "Indium phosphide photonic integrated circuits for free space optical links," IEEE J. Sel. Top. Quantum Electron. **24**, 6101806 (2018).
22. W. W. Chow, M. Lorke, and F. Jahnke, "Will quantum dots replace quantum wells as the active medium of choice in future semiconductor lasers?" IEEE J. Sel. Top. Quantum Electron. **17**, 1349–1355 (2011).
23. J. Lee, M. Devre, B. Reelfs, D. Johnson, J. Sasserath, F. Clayton, D. Hays, and S. Pearton, "Advanced selective dry etching of GaAs/AlGaAs in high density inductively coupled plasmas," J. Vac. Sci. Technol. A **18**, 1220–1224 (2000).
24. S. A. Moore, L. O'Faolain, M. A. Cataluna, M. B. Flynn, M. V. Kotlyar, and T. F. Krauss, "Reduced surface sidewall recombination and

diffusion in quantum-dot lasers," IEEE Photon. Technol. Lett. **18**, 1861–1863 (2006).
25. G. P. Agrawal and N. A. Olsson, "Self-phase modulation and spectral broadening of optical pulses in semiconductor laser amplifiers," IEEE J. Quantum Electron. **25**, 2297–2306 (1989).
26. K. Sato, A. Hirano, and H. Ishii, "Chirp-compensated 40-GHz mode-locked lasers integrated with electroabsorption modulators and chirped gratings," IEEE J. Sel. Top. Quantum Electron. **5**, 590–595 (1999).
27. P. Morton, V. Mizrahi, G. Harvey, L. Mollenauer, T. Tanbun-Ek, R. Logan, H. Presby, T. Erdogan, A. Sergent, and K. Wecht, "Packaged hybrid soliton pulse source results 70 terabit. km/sec soliton transmission," IEEE Photon. Technol. Lett. **7**, 111–113 (1995).
28. A. Hou, R. Tucker, and G. Eisenstein, "Pulse compression of an actively modelocked diode laser using linear dispersion in fiber," IEEE Photon. Technol. Lett. **2**, 322–324 (1990).
29. J. Wiesenfeld, M. Kuznetsov, and A. Hou, "Tunable, picosecond pulse generation using a compressed, modelocked laser diode source," IEEE Photon. Technol. Lett. **2**, 319–321 (1990).
30. M. J. Strain, P. M. Stolarz, and M. Sorel, "Passively mode-locked lasers with integrated chirped bragg grating reflectors," IEEE J. Quantum Electron. **47**, 492–499 (2011).
31. Y. Silberberg and P. Smith, "Subpicosecond pulses from a mode-locked semiconductor laser," IEEE J. Quantum Electron. **22**, 759–761 (1986).
32. T. Schrans, R. Salvatore, S. Sanders, and A. Yariv, "Subpicosecond (320 fs) pulses from CW passively mode-locked external cavity two-section multiquantum well lasers," Electron. Lett. **28**, 1480–1482 (1992).
33. M. Bagnell, J. Davila-Rodriguez, A. Ardey, and P. Delfyett, "Dispersion measurements of a 1.3 μm quantum dot semiconductor optical amplifier over 120 nm of spectral bandwidth," Appl. Phys. Lett. **96**, 211907 (2010).
34. Y. Bidaux, K. A. Fedorova, D. A. Livshits, E. U. Rafailov, and J. Faist, "Investigation of the chromatic dispersion in two-section InAs/GaAs quantum-dot lasers," IEEE Photon. Technol. Lett. **29**, 2246–2249 (2017).
35. D. Pastor, J. Capmany, D. Ortega, V. Tatay, and J. Mart, "Design of apodized linearly chirped fiber gratings for dispersion compensation," J. Lightwave Technol. **14**, 2581–2588 (1996).
36. W. W. Chow, S. Liu, Z. Zhang, J. E. Bowers, and M. Sargent, "Multimode description of self-mode locking in a single-section quantum-dot laser," Opt. Express **28**, 5317–5330 (2020).